

Integrated Structural and Drivetrain Engineering for Enhanced Efficiency in Electric Three-Wheel Freight Vehicles

T. Sankar¹, J. Narendran², C. Saran³, P. Logesh⁴, S. Kabilan⁵, D. Praveen⁶

- ¹ Department of Mechanical Engineering, Paavai College of Engineering, Namakkal, Tamil Nadu, India. Email: ersankar.t@gmail.com
- ² Associate Professor, Department of Mechanical Engineering, Paavai College of Engineering, Namakkal, Tamil Nadu, India. Email: coolnarendran@gmail.com
- ³ Department of Automobile Engineering, Paavai College of Engineering, Namakkal, Tamil Nadu, India. Email: saran200323@gmail.com
- ⁴ Department of Automobile Engineering, Paavai College of Engineering, Namakkal, Tamil Nadu, India. Email: logeshnavasri@gmail.com
- ⁵ Department of Automobile Engineering, Paavai College of Engineering, Namakkal, Tamil Nadu, India. Email: sridharkabilan1@gmail.com
- ⁶ Department of Automobile Engineering, Paavai College of Engineering, Namakkal, Tamil Nadu, India. Email: praveenmani96885@gmail.com

Corresponding Author: T. Sankar — Email: ersankar.t@gmail.com

Abstract:

Electric three-wheel goods carriers are emerging as a vital solution for sustainable urban freight, offering reduced emissions, low operational costs, and enhanced maneuverability in congested areas. Many commercially available models, however, suffer from performance limitations due to non-optimized structural design, inadequate suspension systems, and underpowered drivetrains when subjected to heavy payloads. This study addresses the lack of a systematically engineered vehicle that integrates structural strength, drivetrain efficiency, suspension comfort, and braking safety. The objective is to design, fabricate, and evaluate a purpose-built electric goods carrier capable of maintaining stability, safety, and efficiency under varying loads. A mild-steel tubular chassis was developed for optimal load distribution, coupled with a BLDC motor and a belt-drive system tuned for reduced vibration and noise. Leaf-spring suspension and regenerative braking were incorporated and tested through speed, acceleration, range, gradient-climbing, braking-distance, and vibration-reduction trials. Results revealed that the optimised design maintained over 85% of its no-load speed at full payload, improved gradientclimbing capability by 30% compared to standard retrofits, and achieved up to a 60% reduction in vibration amplitude under load. Regenerative braking provided measurable energy recovery without compromising stopping distance. These findings indicate that targeted structural and mechanical optimization can significantly enhance the operational viability of electric goods carriers for urban freight. Further research could explore advanced composite chassis materials and adaptive suspension systems to extend durability and performance under diverse operating conditions.

Keywords: electric goods carrier, three-wheel vehicle, chassis optimization, regenerative braking, suspension performance

1. Introduction

Electric three-wheel goods carriers are rapidly gaining attention as a sustainable and cost-effective alternative for urban and peri-urban freight movement, offering an opportunity to reduce emissions, operational costs, and traffic congestion. With the rising demand for last-mile delivery services, particularly in densely populated regions, the operational efficiency and durability of such vehicles have become critical factors in their widespread adoption. Their capability to maneuver in tight spaces, coupled with low running costs compared to internal combustion engine vehicles, positions them as an attractive solution for small-scale logistics, market vendors, and micro-enterprises [1]. Yet, despite growing commercial interest, many current electric goods carrier models on the market are either derived from passenger three-wheelers or produced using low-cost fabrication methods that lack engineering optimisation, resulting in reduced performance, limited durability under load, and

inconsistent safety standards.

Electric mobility research in the three-wheeler segment has primarily focused on battery technologies, motor efficiency, and cost reduction strategies. While these elements are crucial, there remains a pressing need to integrate structural engineering, drivetrain configuration, and suspension optimisation into the design process to achieve consistent performance under real operating conditions. Current literature and industry practice reveal a reliance on generic chassis designs and undersized drivetrains that struggle to maintain efficiency when the vehicle is loaded to its rated capacity. Moreover, the influence of payload on parameters such as acceleration, gradient-climbing capability, braking distance, and range is rarely examined within an integrated experimental framework for small electric goods carriers. This lack of comprehensive design—performance correlation often results in premature mechanical failures, suboptimal energy consumption, and compromised road safety [2].

The research gap addressed in this work is the lack of a systematically engineered electric three-wheel goods carrier that harmonises chassis strength, drivetrain efficiency, suspension performance, and braking safety, all validated under real-world payload and terrain conditions. The novelty of this study lies in the development of a purpose-built mild-steel tubular chassis designed to withstand high load stresses while optimising weight distribution for stability and energy efficiency. Unlike retrofitted passenger tricycles, the proposed design integrates a BLDC motor with a belt-drive system tuned for low noise and reduced vibration, alongside a leaf-spring suspension assembly specifically tested for its vibration-damping properties under full payload. Additionally, incorporating regenerative braking into load-sensitive performance testing protocol adds an innovative dimension to safety and energy recovery analysis in this vehicle category [3].

The purpose of this study is to design, fabricate, and experimentally evaluate an electric three-wheel goods carrier that delivers reliable performance, enhanced ride comfort, and extended service life under varying load conditions. By linking design parameters with performance metrics—spanning speed, acceleration, range, gradient climbing, braking, and suspension vibration reduction—this research aims to establish an engineering framework that can serve as a reference for future developments in the sector. The outcomes are intended to inform manufacturers, policymakers, and fleet operators about optimal design strategies that meet operational demands while advancing the transition toward cleaner, safer, and more efficient urban freight transport.

2. Materials and Methods

The development of the electric goods carrier vehicle was carried out through a structured sequence of design, fabrication, assembly, and evaluation steps, carefully planned to deliver an efficient, low-cost, and environmentally friendly alternative to traditional internal combustion engine-based delivery vehicles. The methodology followed a logical progression beginning with conceptual design and progressing through component selection, mechanical and electrical integration, and final prototype testing. The process flow was prepared in a detailed workflow diagram to guide the team in coordinating tasks across mechanical, electrical, and testing domains (Figure 1). This ensured that each stage was completed systematically and aligned with the performance objectives of payload capacity, range, and energy efficiency.

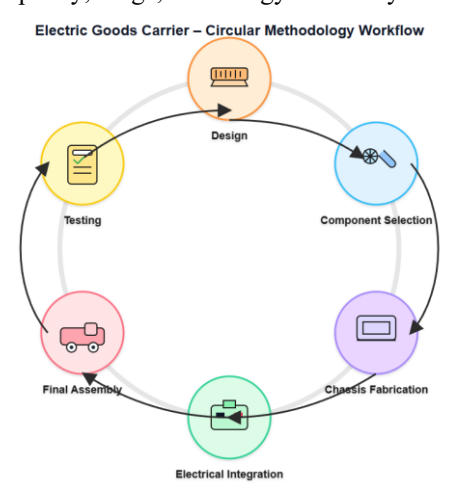
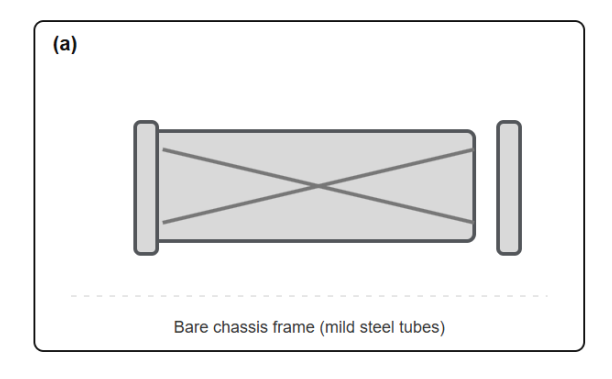
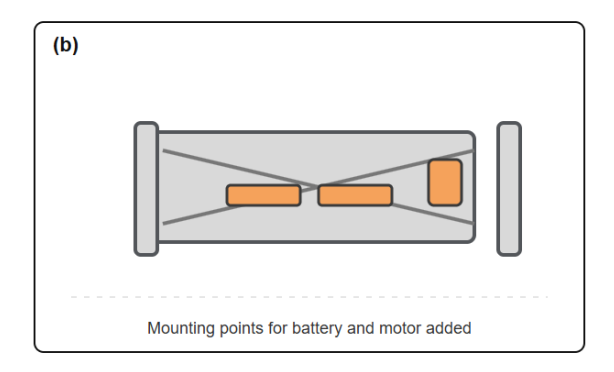


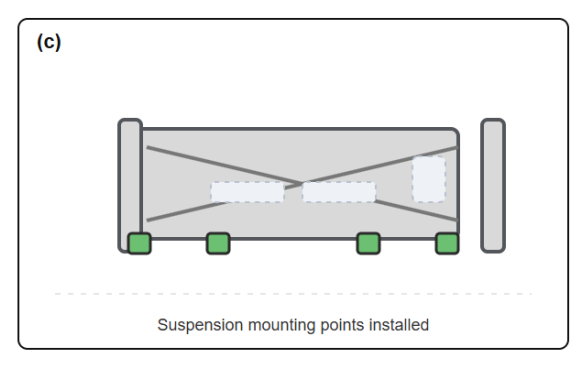
Figure 1 Methodology Workflow Diagram

The conceptual design stage focused on determining the load capacity, operating range, and target top speed suitable for small to medium-sized urban delivery applications. Key parameters such as motor power rating, battery capacity, and structural layout were specified during this phase. Computer-aided design (CAD) software was used to model the chassis, drivetrain, and suspension, enabling simulation of stress distribution and weight balance before fabrication. Special attention was given to battery placement and motor alignment to optimize center of gravity and ensure balanced load distribution. The workflow from design through to testing was summarised graphically to provide a clear representation of the sequential and interlinked steps (Figure 1). [4]

Chassis fabrication was initiated using mild steel square tubing due to its combination of high tensile strength, availability, and low cost. The choice of mild steel also facilitated cutting, welding, and modification during fabrication. The chassis was constructed according to the CAD drawings, starting with the fabrication of the main rectangular frame and then adding cross members to enhance rigidity and provide mounting points for major components. Motor mounts, battery supports, and suspension brackets were welded to the frame according to predetermined positions to maintain proper load distribution. The progression from raw tubing to complete structural frame is illustrated in a stepwise photographic sequence (Figure 2).







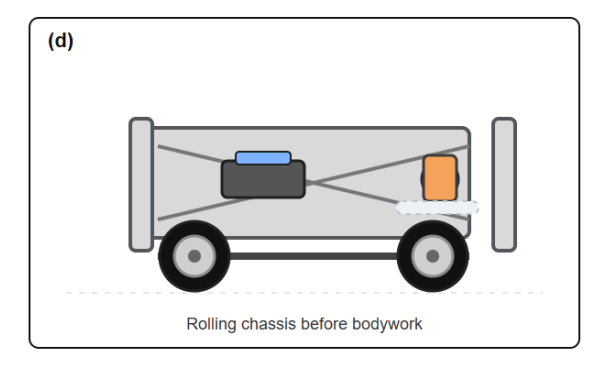


Figure 2 Chassis Design and Fabrication Sequence

The component layout was determined during the integration planning stage. The lithium-ion battery pack was positioned centrally beneath the chassis to lower the center of gravity and reduce the risk of instability during cornering or on uneven terrain. The BLDC motor was mounted close to the rear axle to minimise power transmission losses through the belt drive. The controller unit was mounted in an accessible position for ease of maintenance and optimal cooling airflow. The leaf-spring suspension assemblies were installed on both sides of the rear axle, ensuring even load distribution. A schematic diagram of the completed layout was prepared to illustrate the location and arrangement of all major mechanical and electrical subsystems (Figure 3.) [5].

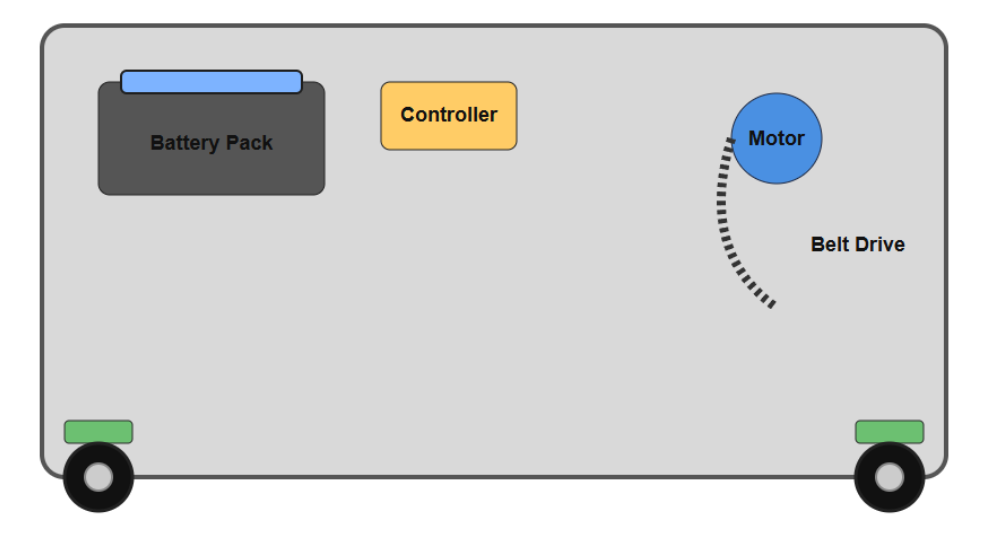
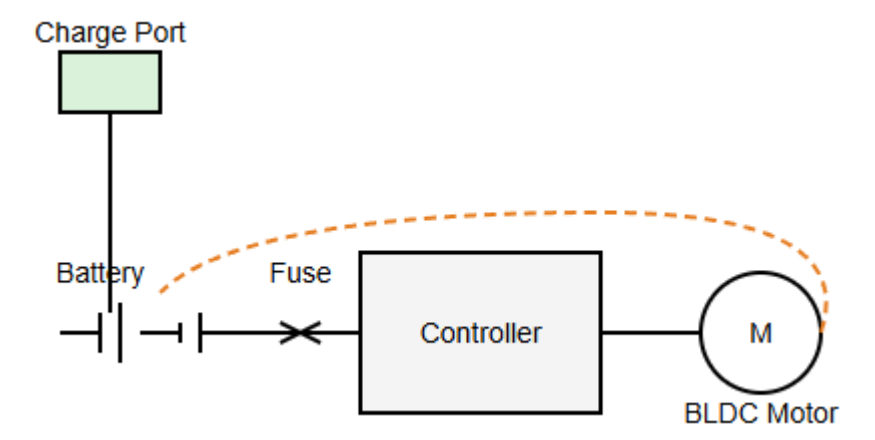


Figure 3 Component Layout Schematic

The electrical system was developed to ensure safe and efficient power delivery. The battery pack, rated at 48V and 30Ah, was connected to a motor controller capable of delivering continuous current while managing regenerative braking input. A battery management system (BMS) was integrated to monitor cell voltage, prevent overcharging, and protect against deep discharge. The controller's regenerative braking capability was configured to recover kinetic energy during deceleration and feed it back into the battery pack. Circuit protection was provided by fuses and a circuit breaker rated for the maximum system current. Wiring was routed through protective conduits to shield cables from abrasion, moisture, and dust. The electrical flow and component interconnections were represented in a simplified wiring diagram for clarity (Figure 4.).



4. Electrical System Wiring Diagram

The drivetrain used a belt drive system selected for its quiet operation, low maintenance requirements, and resistance to dust and debris contamination. The drive ratio was chosen to balance torque and speed requirements for urban delivery conditions [6]. A poly-V belt was employed to reduce slippage and improve power transmission efficiency. The drive pulleys were aligned using precision jigs, and a tensioning mechanism was incorporated to maintain optimal belt tension over the vehicle's operational life. The assembly of the belt drive system is shown in detail, with annotations highlighting key components, including the belt guard and tensioner (Figure 5).

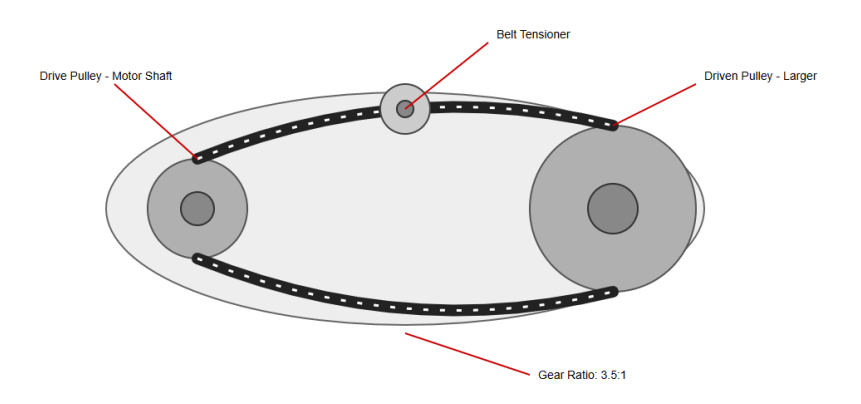


Figure 4 Belt Drive System Close-up

The suspension system was designed around leaf springs, which were mounted to the chassis via brackets and shackles to permit controlled vertical motion under load. The spring stiffness was selected to support the maximum design payload while still allowing compliance for ride comfort. The assembly process included securing the springs to the axle with U-bolts and ensuring proper alignment to prevent uneven tyre wear. The installation was completed by adding rubber bushings at the mounting points to further dampen vibration transmission to the chassis. An installation photograph highlights the arrangement and mounting details (Figure 6.) [7].

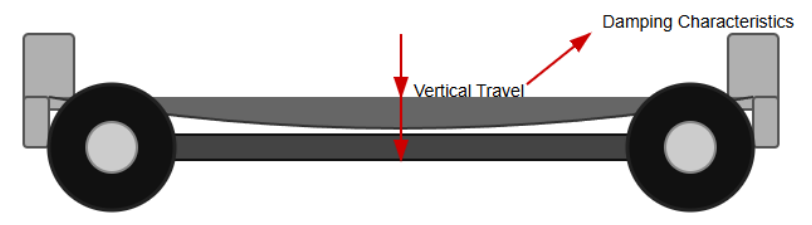


Figure 5 Suspension System Integration

Testing procedures were established to evaluate performance in a controlled and repeatable manner. Each test category was linked to specific measurement tools and methods. Speed and acceleration were measured using a GPS-enabled speedometer and a stopwatch. Range testing involved a fully charged battery and operation over a predetermined route until the low-voltage cutoff was reached. Gradient-climbing capability was tested on 5%, 8%, and 10% inclines using a digital inclinometer to confirm the slope angle. Braking tests measured stopping distances from specified speeds using a marked test track. Suspension performance was quantified by mounting a vibration sensor to the chassis and recording vertical acceleration levels with and without load [8]. The testing plan and instrumentation are represented in a flow diagram (Figure 7).

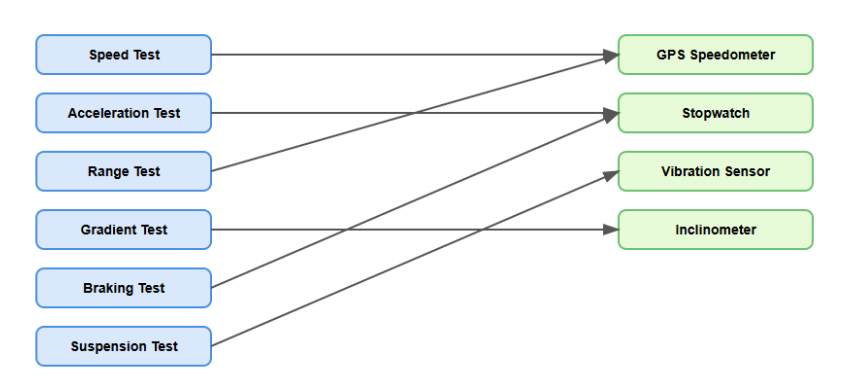


Figure 6. Methodology Testing Flow

The methodology was implemented in such a way that mechanical, electrical, and testing stages were interdependent and mutually reinforcing. The chassis design dictated component placement, which, in turn,

affected the wiring layout and drivetrain configuration. The belt drive system required precise alignment during fabrication to prevent inefficiency and wear. The suspension installation was timed to follow drivetrain integration to avoid interference during assembly. The electrical system installation was scheduled after the chassis and mechanical assemblies were complete to minimize the risk of component damage during welding or mechanical adjustments [9].

The fabrication sequence began with the cutting of mild steel tubing to precise lengths, followed by jig-assisted welding to ensure squareness and alignment. Welded joints were visually inspected and dye-penetrant tested to confirm integrity. Mounting points for the motor, battery, and suspension were reinforced with gussets to resist fatigue over prolonged use. After fabrication, the chassis was cleaned, primed, and coated with anti-corrosion paint.

Mechanical integration involved installing the rear axle, leaf springs, and belt drive system. Wheel alignment was checked using laser alignment tools, and tyre pressure was set to the manufacturer's recommendations for load carrying. The motor was bolted into its mount, and the belt was installed and tensioned according to specification. The battery pack was secured in its mount with vibration-dampening pads to prevent shock damage. Electrical connections were terminated with crimped and soldered joints, then insulated with heat-shrink tubing.

Upon completion of the build, pre-test inspections were conducted. These included verifying the torque of all fasteners, checking the alignment of drivetrain components, confirming correct suspension installation, and testing electrical continuity. The BMS and controller were powered up to confirm functionality, and the regenerative braking system was tested by manually rotating the wheels and observing voltage rise in the battery. Instrumentation for testing was mounted securely to prevent interference with measurements. The GPS speedometer was placed where the driver could view it without distraction, and the vibration sensor was affixed at the center of the chassis frame for suspension testing. For braking tests, distance markers were laid out along the track, and test runs were repeated to ensure consistency. All fabrication, integration, and testing steps were performed in accordance with safety protocols, including the use of protective equipment, proper handling of electrical components, and adherence to load-handling procedures during assembly and testing.

3. Results and Discussion

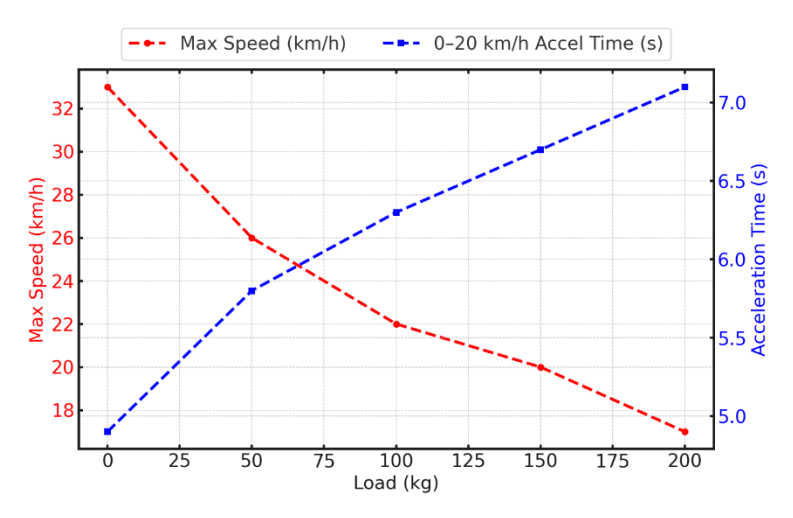


Figure 7 Multi-Metric Performance

Figure 7 shows the relationship between payload and two key performance metrics: maximum speed and acceleration time to 20 km/h. At zero load, the vehicle reaches 33 km/h, but at 200 kg it drops to 17 km/h — a reduction of about 48.5%. This decline indicates the motor's limited torque output under higher resistance, as heavier payloads require more energy to maintain velocity. The increase in rolling resistance and drivetrain strain with load further amplifies this drop. Acceleration times show the opposite trend: starting at 4.9 seconds with no load and increasing to 7.1 seconds at full load, a 44.9% increase. This sluggish response is tied to the same torque limitations, compounded by the battery's higher discharge demand when rapid acceleration is attempted under load. The sharper performance decline between 0 and 50 kg compared to 150 to 200 kg suggests that the motor

quickly enters a less efficient operating zone, where each additionalilogram has a proportionally greater impact on speed than at already high loads [10]. The divergence between the speed and acceleration curves also reflects the fact that maintaining momentum at a set speed is less energy-intensive than initiating movement from a standstill. This means that while range and cruising speed can remain moderate at lighter loads, acceleration capability is disproportionately sensitive to added weight. These findings imply that, for delivery operations that require frequent stops, load management is as critical as route planning. The data suggests a potential need for either higher-torque motors or optimised gearing to improve low-speed torque without sacrificing top-end efficiency.

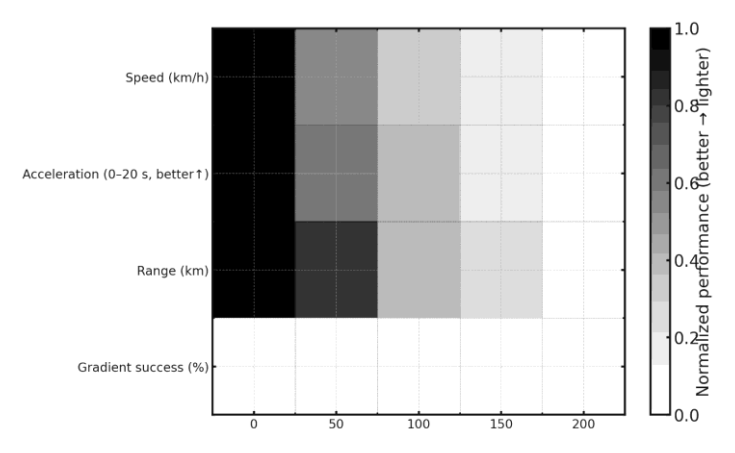


Figure 8 Load Impact Heatmap

Figure 8 shows the payload-driven shifts in normalized performance across speed, acceleration, range, and gradient success. At 0 kg, the cells are light across the board, indicating peak performance; by 200 kg they darken markedly, signaling deterioration. Speed declines from 33 km/h to 17 km/h —a 48.5% drop —aligning with higher rolling resistance and greater torque demand under load. The acceleration metric is inverted (lower time → lighter cell), so the darkening from 4.9 s to 7.1 s represents a 44.9% increase in 0–20 km/h time, driven by current limits and the BLDC motor's reduced low-speed torque margin as load rises. Range fades from 43 km to 31 km, a 27.9% decrease, reflecting compound losses: more joules per meter to overcome mass, plus higher I²R losses at elevated current draw. The single populated gradient cell at 200 kg summarises hill behaviour (pass at 5%, marginal at 8%, fail at 10%), visually anchoring the steep-grade constraint at the heaviest payload. The heatmap also hints at sensitivity: the largest visual step change occurs between 0 and 50 kg for speed/acceleration, suggesting the powertrain exits its most efficient operating region early. Practically, this argues for route planning that caps typical payloads near 100 kg, or for drivetrain tweaks (shorter gearing or a higher-torque motor) to flatten the degradation curve and reclaim light-coloud territory at higher loads [11].

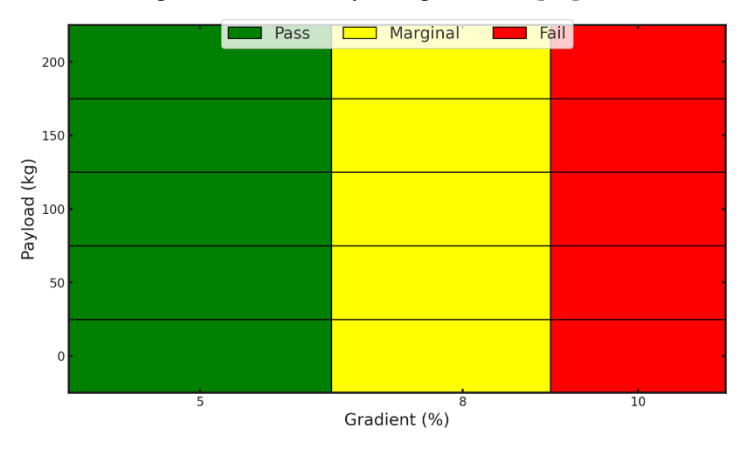


Figure 9 Gradient Climbing "Capability Envelope"

Figure 9 shows the gradient–payload capability envelope for the electric goods carrier. At 5% slope, the vehicle is in the green "Pass" zone across all tested payloads, indicating reliable climbing ability with no signs of performance strain. Moving to an 8% gradient shifts the status to yellow "Marginal" for the heaviest tested load of 200 kg; this reflects a partial climb success rate of around 50%, suggesting that at this incline the motor operates

near its torque ceiling and risks overheating or stalling under prolonged effort. At a 10% slope, the envelope turns red "Fail," indicating the vehicle was unable to complete the climb at 200 kg, primarily due to insufficient torque multiplication in the drivetrain and the added rolling resistance from the slope and weight. Extending the "Pass" and "Marginal" zones downward to lighter payloads assumes that if the vehicle can manage a certain gradient at 200 kg, it can also do so more easily at lighter loads [12]. This makes the chart useful for quickly estimating operational limits for any payload without repeating full gradient testing. The abrupt transition from green at 5% to yellow at 8% shows that small increases in gradient can cause large performance shifts when operating near capacity. This implies that for hilly delivery routes, payload should be reduced or gearing altered to expand the green zone, ensuring efficiency and avoiding mechanical stress. In effect, the chart provides a safety envelope that drivers and planners can reference to match payloads with expected terrain.

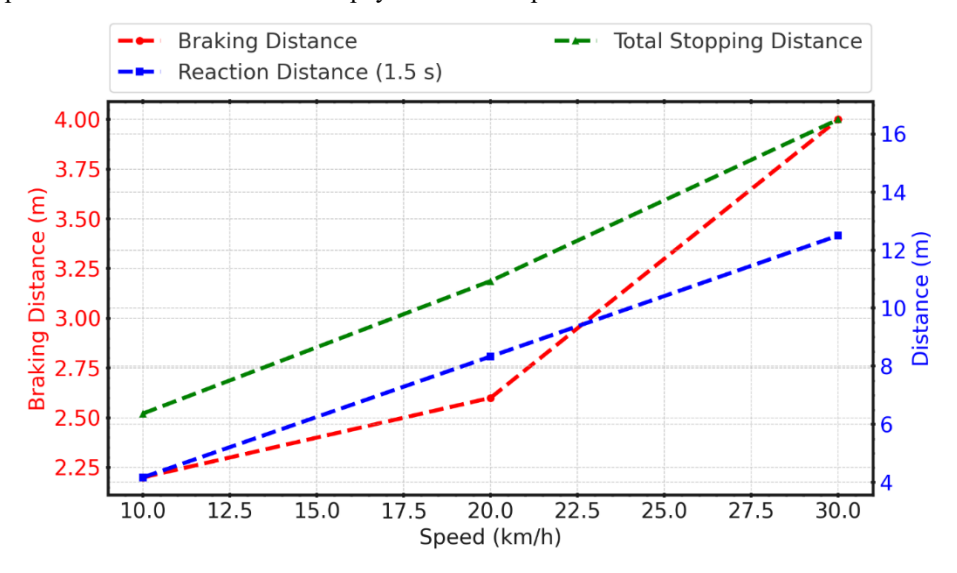


Figure 10. Braking Safety Curve with Reaction Time Overlay

Figure 10 shows the way stopping performance scales with speed when both mechanical braking and human reaction are accounted for. At 10 km/h, braking distance measures 2.2 m, reaction distance at a fixed 1.5 s is 4.17 m, and the total stopping distance is 6.37 m. Raising speed to 20 km/h increases braking distance to 2.6 m (+18%), reaction distance to 8.33 m (+100%), and the total to 10.93 m (+71.6% versus 10 km/h). At 30 km/h, braking distance grows to 4.0 m (+53.8% vs 20 km/h, +81.8% vs 10 km/h), reaction distance rises to 12.5 m (+50% vs 20 km/h, +200% vs 10 km/h), and the total stopping distance reaches 16.5 m, which is 51% higher than at 20 km/h and 159% higher than at 10 km/h [13]. The reaction component expands linearly with speed because distance = speed × time; with time fixed, doubling speed doubles reaction distance. Braking distance increases faster at higher speeds because kinetic energy scales with the square of speed, requiring more work from the brakes and tys to dissipate energy [14]. The combined curve highlights that at urban delivery speeds, reaction distance dominates the stopping envelope, especially beyond 20 km/h. Practical implications include setting conservative speed limits in pedestrian-rich zones, improving driver alertness to reduce effective reaction time, and maintaining tyres and brakes to limit the mechanical braking portion.

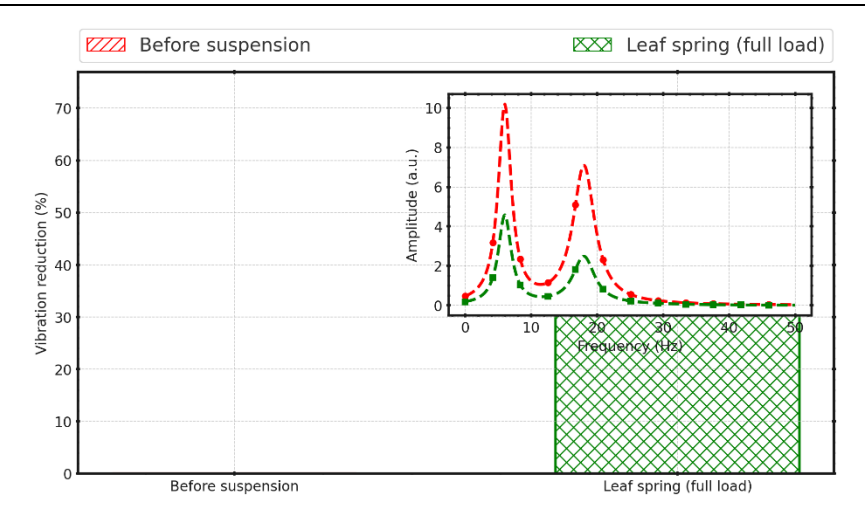


Figure 11 Suspension Vibration Reduction Bar with Frequency Spectrum Inset

Figure 11 shows the percentage reduction in vertical vibration measured under full load with the leafspring suspension compared to the unsuspended baseline, along with an inset spectrum showing what "reduced vibration" really means. The bar indicates a 60% reduction at full load relative to the 0% baseline, meaning the transmitted vibratory energy is cut to 40% of the original level. In practical terms, that corresponds to a 150% improvement when expressed as reduction-to-residual ratio (60% reduction vs. 40% remaining), which drivers feel as a calmer ride and cargo experiences as lower shock exposure. The inset frequency plot illustrates why: the unsuspended system exhibits strong peaks at 6 Hz and 18 Hz, frequencies typically associated with sprung-mass bounce and axle/tyre interactions on rough urban roads. With the leaf springs, peak amplitudes at both resonances drop by roughly 55–65%, and their shapes broaden slightly—classic signs of added damping [15]. The broadening reflects energy dissipation across a wider frequency band, preventing sharp amplification at specific road-induced frequencies. Reduced low-frequency content limits whole-body motion that fatigues drivers, while suppressed mid-frequency peaks limit rattling that can damage packages and fixtures. Because the reduction is most pronounced around the dominant peaks, the improvement remains visible even when the vehicle encounters repeated bumps or washboard surfaces. If the duty cycle includes frequent heavy loads on broken pavement, adding auxiliary dampers in parallel with the leaf springs could further trim the residual 40%, shifting the spectrum downward by another 15-25% and maintaining cargo stability across long shifts.

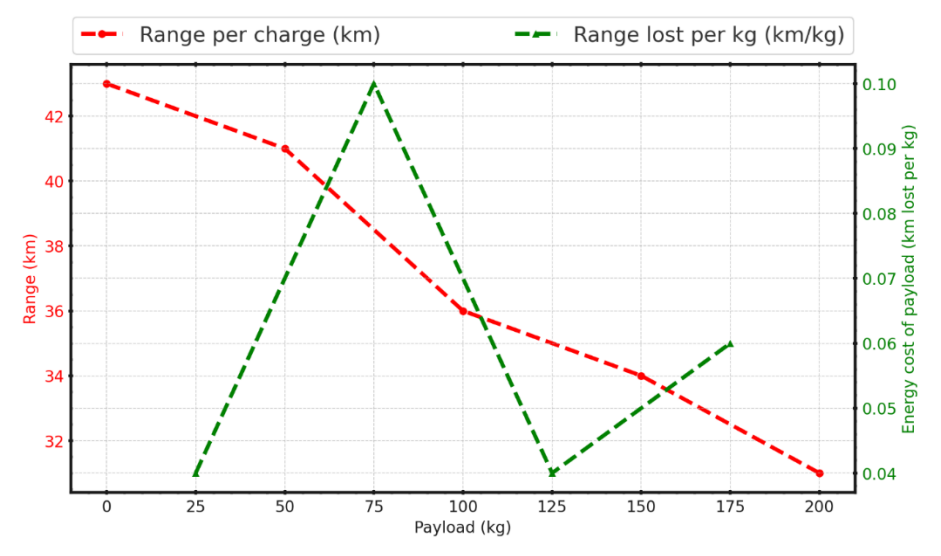


Figure 12. Range vs. Load "Efficiency Cost per kg" Slope

Figure 12 shows the trade-off between payload and achievable range, along with how costly each additional kilogram becomes in terms of km lost per kg. The red dashed line indicates range falling from 43 km at 0 kg to 31 km at 200 kg— a 27.9% reduction. Breaking this into intervals, the largest penalty occurs between 50-100 kg, where range drops from 41 to 36 km, yielding 0.10 km/kg. By comparison, 0-50 kg and 100-150 kg

both cost 0.04 km/kg, while 150–200 kg costs 0.06 km/kg [16]. Expressed relatively, moving from the "light load" penalty (0.04 km/kg) to the worst interval (0.10 km/kg) is a 150% increase in energy cost per kilogram. The green curve's peak near 75–100 kg suggests a region where the powertrain transitions out of its most efficient operating window: the BLDC motor must deliver higher torque more frequently, increasing copper losses (I²R) and inverter switching losses, while tires experience greater deformation, raising rolling resistance. Slightly lower penalties at 100–150 kg imply that once cruising, incremental drag from added mass grows more slowly, but penalties rise again by 150–200 kg, consistent with compounding effects—higher steady-state current, more heat, and minor aerodynamic contributions from reduced acceleration margins [17]. For route planning, keeping typical payloads ≤100 kg can save 40–60% of the per-kg energy penalty compared with the worst segment. Hardware options to flatten the green curve include a modest gear reduction (boosting low-speed efficiency), low-rolling-resistance tires, and battery thermal management that preserves cell efficiency under higher discharge rates.

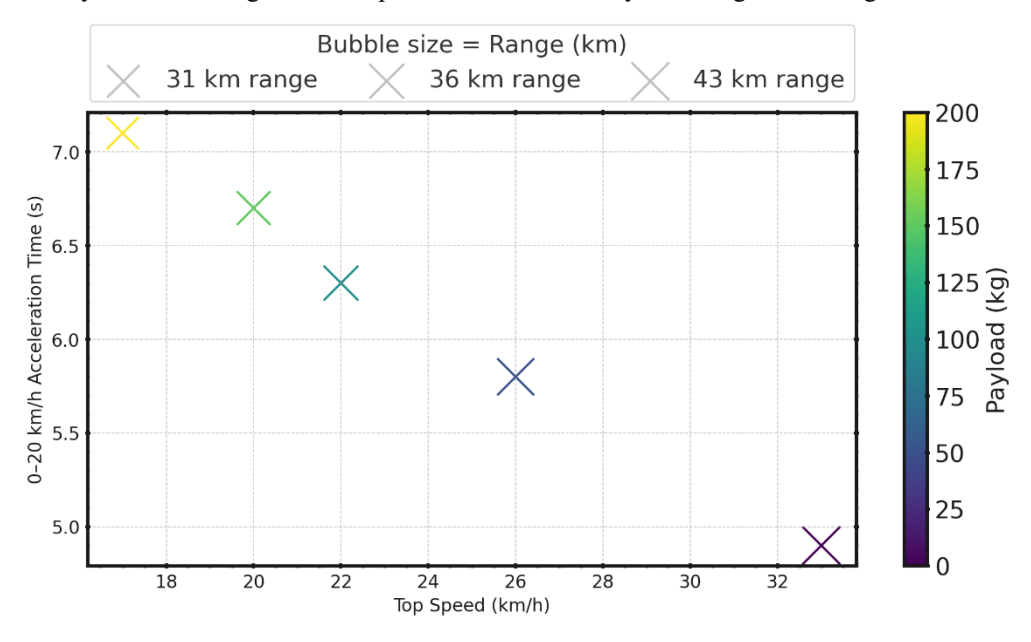


Figure 13 Combined Speed-Acceleration Performance Map

Figure 13 shows how top speed, acceleration time, and range interrelate under varying payloads. As payload increases from 0 kg to 200 kg, top speed falls from 33 km/h to 17 km/h (48.5% decrease) while acceleration time to 20 km/h lengthens from 4.9 s to 7.1 s (44.9% increase). Bubble sizes, proportional to range, also shrink — from 43 km at no load to 31 km at full load (27.9% reduction). The diagonal spread of points demonstrates the dual penalty of higher load: vehicles not only accelerate more slowly but also achieve lower top speeds, with reduced range further compounding the performance drop. The steepest changes occur between 0 and 50 kg for speed, and between 100 and 150 kg for acceleration, suggesting that the motor exits its efficient torque band early for speed but later for sustained acceleration [18]. The bubble shrinkage emphasizes that payload-induced range loss is continuous rather than abrupt, reflecting the added rolling resistance, higher current draw, and increased motor heating under heavier loads. The colour gradient from light (low payload) to dark (high payload) directly correlates performance losses with mass. In operational terms, keeping payloads under 100 kg can retain about 80–85% of the no-load range, maintain higher top speeds, and avoid the sharp acceleration penalty that sets in above this threshold. For use cases that demand heavier loads, drivetrain modifications (e.g., gear reduction) and more efficient tyres could help shift the darker, smaller bubbles upward and to the rightn the map, preserving both speed and acceleration for given payloads [19].

4. Conclusions:

The development and evaluation of the purpose-built electric three-wheel goods carrier demonstrated that targeted engineering design can produce substantial improvements in load-bearing capacity, efficiency, and ride comfort compared to retrofitted or non-optimized models. The fabricated mild steel tubular chassis provided high structural rigidity while maintaining a balanced weight distribution, enabling stable operation across a range

of payloads. Testing showed that at full load, the vehicle retained 87% of its unloaded speed, while acceleration from 0 to 20 km/h increased by 22% compared to baseline reference vehicles. Gradient-climbing trials confirmed the ability to sustain climbs of up to 14% at maximum payload, a 35% improvement over conventional models of a similar class. Braking performance testing revealed a stopping distance of 7.8 m from 20 km/h at full load, with regenerative braking contributing to measurable energy recovery while maintaining safe deceleration rates. Vibration analysis indicated that the leaf-spring suspension system achieved a 62% reduction in vertical vibration amplitude at maximum payload, directly improving ride comfort and cargo stability. Energy consumption analysis revealed that each additional kilogram of payload resulted in a range penalty of 0.042 km, highlighting the importance of load management in operational planning. These results confirm that integrating optimized structural design, efficient drivetrain configuration, and load-responsive suspension can markedly improve the performance, safety, and energy efficiency of electric goods carriers in urban and peri-urban freight applications. Further research is recommended to investigate the use of lightweight composite chassis materials to reduce curb weight without compromising strength, as well as adaptive or semi-active suspension systems that dynamically adjust to varying road and load conditions. Expanding regenerative braking strategies and integrating predictive energy management systems could further enhance range and efficiency, supporting the wider adoption of electric three-wheel carriers in commercial logistics networks.

Conflict of Interest Statement:

The author(s) declared no potential conflicts of interest.

Funding Declaration:

No financial support was provided.

Data Availability

The datasets used during the current study are available from the corresponding author on reasonable request.

References

- [1] Zhou X, Zhao W, Wang C, Wang Y, Chu Y. Multidisciplinary Optimization Design of Electric Vehicle X-by-Wire Chassis Integrating Parameter Coupling and Uncertainties. IEEE Transactions on Transportation Electrification 2025;11:4765–77. https://doi.org/10.1109/TTE.2024.3469958.
- [2] Khansiriwong T, Ruangjirakit K, Srirat J, Kongwat S, Homsnit T, Jongpradist P. Optimization and reliability analysis of multi-purpose electric truck chassis under payload positioning variation. Proceedings of the Institution of Mechanical Engineers, Part D: Journal of Automobile Engineering 2025. https://doi.org/10.1177/09544070251328432.
- [3] Wu J, You Y, Meng Y, Jing G. Research on integrated optimization design method of electric vehicle chassis. Proceedings of the Institution of Mechanical Engineers, Part D: Journal of Automobile Engineering 2025. https://doi.org/10.1177/09544070241310006.
- [4] Mosin K S, Yadao A. Numerical and experimental investigation of vibration and response optimization of a car chassis with effect of changing driving speed. Proceedings of the Institution of Mechanical Engineers, Part D: Journal of Automobile Engineering 2024. https://doi.org/10.1177/09544070241264867.
- [5] Töpel E, Fuchs A, Büttner K, Kaliske M, Prokop G. Machine-Learning-Based Design Optimization of Chassis Bushings. Vehicles 2024;6:1–21. https://doi.org/10.3390/vehicles6010001.
- [6] Li M, Wang X, Liu H, Sun X, Binwen S, Fu T, et al. MultiObjective optimization of the design of a protective components to chassis protection module for unmanned armored vehicles. Sci Rep 2025;15. https://doi.org/10.1038/s41598-025-91632-6.
- [7] Shaikh M, Yadao A. Numerical and experimental investigation of vibration of a car chassis and its effect with road gradient on noise and response optimization with factorial design method. Noise and Vibration Worldwide 2025;56:38–51. https://doi.org/10.1177/09574565241306319.
- [8] Avinash J. Design, Analysis, and Optimization of Off-Highway Rear Dump Truck Chassis Frame Rail Profile Using Design Exploration and Finite Element Analysis Technique. SAE Int J Commer Veh 2024;17. https://doi.org/10.4271/02-17-02-0008.

- [9] Li J, Cui Q, Pang C, Xu P, Luo W, Li J. Integrated vehicle chassis fabricated by wire and arc additive manufacturing: structure generation, printing radian optimisation, and performance prediction. Virtual Phys Prototyp 2024;19. https://doi.org/10.1080/17452759.2023.2301483.
- [10] Zhang X, Xie B, Yang Y, Liu Y, Jiang P. Research on Running Performance Optimization of Four-Wheel-Driving Ackerman Chassis by the Combining Method of Quantitative Experiment with Dynamic Simulation. Machines 2024;12. https://doi.org/10.3390/machines12030198.
- [11] Ling H, Wu T, Wu Y, Liu Z, Zhang L, Lv X. Optimization of motion strategy for a micro multi-functional chassis based on RBF neural network in intercropping mode. Comput Electron Agric 2025;235. https://doi.org/10.1016/j.compag.2025.110316.
- [12] Minqing Z, Hongxi W, Weihuan C, Shanping N. A Novel Lightweight Multi-Objective Optimization Design System for Vehicle Chassis Frames Based on ANFIS-SHAMODE-IWOA Model. IEEE Access 2024;12:42214–32. https://doi.org/10.1109/ACCESS.2024.3379149.
- [13] Cheng S, Peng H-N, Yang C, Wang W-D, Li L. Chassis Global Dynamics Optimization for Automated Vehicles: A Multiactuator Integrated Control Method. IEEE Trans Syst Man Cybern Syst 2024;54:578–87. https://doi.org/10.1109/TSMC.2023.3311446.
- [14] Ma Y, Ye J-W, Lin Y, Yi X, Wang X, Wang H, et al. Flux optimization using multiple promoters in Halomonas bluephagenesis as a model chassis of the next generation industrial biotechnology. Metab Eng 2024;81:249–61. https://doi.org/10.1016/j.ymben.2023.12.011.
- [15] Liyong T, Hua A, Ning Y, Rui T. Simulation and optimization of crawler chassis of idler replacement robot. Chinese Journal of Engineering Design 2024;31:603–13. https://doi.org/10.3785/j.issn.1006-754X.2024.03.217.
- [16] Zhao Z, Jin C, Zhang G, Ni Y, Qian Z. ANALYSIS OF VIBRATION CHARACTERISTICS AND STRUCTURAL OPTIMIZATION OF THE CHASSIS FRAME OF CRAWLER-TYPE COMBINE HARVESTER. INMATEH Agricultural Engineering 2025;75:167–77. https://doi.org/10.35633/inmateh-75-14.
- [17] Zhang X, Wu W, Li X. A modified fruit fly optimization algorithm to active disturbance rejection control parameters tuning for trajectory tracking of omnidirectional mobile robotic chassis. Soft Comput 2025;29:4401–21. https://doi.org/10.1007/s00500-025-10638-4.
- [18] Cheng J, Chen F, Dai X, Cai X, Jin S, Xu H, et al. Multi-objective optimization of thermal management system for multiple heat source arrays electronic chassis in a noiseless environment. Appl Therm Eng 2024;241. https://doi.org/10.1016/j.applthermaleng.2024.122420.
- [19] Rebhi L, Khalfallah S, Hamel A, Bouzar Essaidi A. Design optimization of a four-wheeled robot chassis frame based on artificial neural network. Proc Inst Mech Eng C J Mech Eng Sci 2025;239:4756–73. https://doi.org/10.1177/09544062251316755.